Journal of Materials Chemistry C

Bimolecular crystal instability and morphology of bulk heterojunction blends in organic and perovskite solar cells

Journal:	*Journal of Materials Chemistry C*
Manuscript ID	TC-ART-04-2020-002030.R1
Article Type:	Paper
Date Submitted by the Author:	25-May-2020
Complete List of Authors:	Song, Jingnan; Shanghai Jiao Tong University Hu, Qin; University of Massachusetts Amherst; Lawrence Berkeley National Laboratory Zhang, Ming; Shanghai Jiao Tong University Zhang, Quanzeng; Shanghai Jiao Tong University, Zhu, Lei; Shanghai Jiao Tong University, Ali, Jazib; Shanghai Jiao Tong University, School of physics Wang, Cheng; The Lawrence Berkeley National Laboratory, Advanced Light Source Feng, Wei; National Key Laboratory of Fluorinated Materials Russell, Thomas; University of Massachusetts Amherst; Lawrence Berkeley National Laboratory Liu, Feng; Shanghai Jiao Tong University,

Bimolecular crystal instability and morphology of bulk heterojunction blends in organic and perovskite solar cells

Jingnan Song[a], Qin Hu[b, c], Ming Zhang[a], Quanzeng Zhang[a], Lei Zhu[a], Jazib Ali[a], Cheng Wang[d], Wei Feng[e], Thomas Russell*[b, c] and Feng Liu*[a]

[a]Frontiers Science Center for Transformative Molecules, School of Chemistry and Chemical Engineering, Shanghai Jiao Tong University, Shanghai 200240, China

[b]Department of Polymer Science and Engineering, University of Massachusetts, Amherst, MA 01003, USA

[c]Materials Sciences Division, Lawrence Berkeley National Laboratory, Berkeley, California 94720, USA

[d]Advanced Light Sources, Lawrence Berkeley National Laboratory, Berkeley, California 94720, USA

[e]State Key Laboratory of Fluorinated Materials, Zibo City, Shandong 256401, China.

*Address correspondence to: tom.p.russell@gmail.com, fengliu82@sjtu.edu.cn

Abstract

The performance of polymer:fullerene bulk heterojunction (BHJ) solar cells is significantly influenced by the morphology of electron donor and acceptor blends under the premise that electronic structure is complimentary regarding to donor and acceptor materials. There are many cases where intimate mixing of donor and acceptor perturbs the electronic structure, which fundamentally changes the transport and photovoltaic characteristics. Here, we present the bimolecular crystal packing of polymers and fullerenes, and investigate the correlation between device performance and structural details. We find that bimolecular crystallization can reorganize polymer chain packing, leading to poor electron transport and device performance. The size compatibility and the passivation of entropy penalty led to cocrystallization instability, which was clearly seen by *in situ* GIWAXS data. $PC_{61}BM$ is found to intercalate into side chains of PQT by reorganizing both PQT and $PC_{61}BM$, forming a stable, highly ordered bimolecular crystals. The poor electron transport in bimolecular crystal domain could account for the poor device performance in both perovskite and organic solar cells. Bis-$PC_{61}BM$, on the other hand, only forms loosely packed aggregates in solution, and then rapidly phase separated into large domains with an edge-on interfacial orientation and performed poorly in solar cells.

Introduction

Blending an organic semiconducting donor with an acceptor, in general, leads to a phase separated bulk heterojunction (BHJ) morphology, which can increase interfacial area and independent electron and hole transport domains, and favorable for photovoltaic applications, yielding reported power conversion efficiencies of up to ~16% in single layered solar cells [1-5]. The transport and performance of BHJ solar cells are heavily influenced by the nanoscopic structure of the donor:acceptor blends, where domain size and purity, ordering and orientation of components within the domain, and the characteristics of the interface between the domains that dictates exciton dissociation, recombination and charge transport [6-11]. Generally, a bicontinous morphology with domains tens of nanometers in size, where the domains are either pure donor or acceptor, is desirable to balance exciton splitting and carrier hopping. Partial mixing of the donor and acceptor is generally considered to be detrimental to the performance. Although there are cases where the donor and acceptor form guest-host bimolecular crystals, that can decrease performance, manipulation and optimization of the morphology is still challenging [12-16]. One case in point are mixtures of poly(2,5-bis(3-tetradecyllthiophen-2-yl)thieno[3,2-b]thiophene) (PBTTT) and phenyl-c71-butyric acid methyl ester ($PC_{71}BM$) where the PBTTT side chain can host $PC_{71}BM$, suppress the stacking of the polymer chains, forming bimolecular crystals at the eutectic temperature [12, 17]. Guest-host size and temperature are determining factors that guide the bimolecular crystallization, which in-turn, affect the performance of photovoltaic devices [18, 19].

Revealing the structure and morphology of the blends at all length scales and at interfaces, and relating these to the transport and photovoltaic properties, is of great interest for adding new insights into organic semiconducting materials. Poly(3, 3'-didodecylquaterthiophene) (PQT) is a well-established hole-transporting semi-crystalline polymer that has large side-chain vacancies to accommodate guest molecules. Highly ordered crystalline packing can be produced by side-chain interdigitation [20-22]. However, this is not a good photovoltaic material, showing a low power conversion efficiency (PCE) of only ~0.4% [23, 24]. Whether the poor performance is a result of the intrinsic properties of PQT or the morphology is an open question. To address this, we performed morphological studies on the bimolecular crystallization of PQT and mono-/bis-fullerene adducts using scattering and imaging methods and correlated this to their performance in organic solar cells. The miscibility of PQT with the mono- and bis-fullerene adducts was found to be different, leading to distinctly different phase separation behavior and interfacial orientation. Size compatibility was found to be a major factor in governing the bimolecular intercalation in thin film blends. In wet films, the bis-fullerene

adduct can form an ordered bimolecular structure, that rearranged as the solvent evaporated. The bimolecular crystals are not efficient electron transporters, requiring excessive amounts of $PC_{61}BM$ to function.

Results and Discussions

Fig. 1a and b shows the chemical structures of PQT, $PC_{61}BM$, and Bis-$PC_{61}BM$, as well as the UV-vis absorption spectra. The polythiophene backbone and regularly spaced dodecyl side chains make it a good host for fullerene molecules. In neat thin films, a semi-crystalline π–π stacked lamellar morphology forms good transport channels; partial interdigitation of the side-chains from adjacent lamellae occurs in PQT, promoting three dimensional order [20]. Absorption spectra of pure PQT, PQT:fullerene ($PC_{61}BM$ and Bis-$PC_{61}BM$) blends with different weight ratios are shown in Fig. 1b. Here, the 1:1 and 1:4 weight ratios of PQT and $PC_{61}BM$ are abbreviated as PQT-M1 and PQT-M2, and the 1:1 and 1:4 weight ratios of PQT and Bis-$PC_{61}BM$ are abbreviated as PQT-M3 and PQT-M4. The pure PQT film exhibits a strong absorption in the range from 400 to 625 nm, with a well-resolved resonant shoulder at ~600 nm, attributed to the ordering of PQT chains. When PQT is blended with $PC_{61}BM$, the resonance structure is disrupted, indicating a fundamental change in electronic structure. The 600 nm shoulder peak in PQT-M2 blends disappears, so the π–π stacking of PQT is also disrupted. This is similar to the results found in PBTTT:$PC_{71}BM$ blends [14]. PQT:Bis-$PC_{61}BM$ blends show a similar absorption as PQT in neat films with good structure resonance. Therefore, PQT-PQT contacts are maintained.

Grazing incidence wide-angle x-ray scattering (GIWAXS) was used to study the molecular packing and crystallization of PQT:fullerene blends. As shown in Fig. 1c and Fig. S1, PQT crystallizes, with the (100) peak at 0.32 $Å^{-1}$ (with crystal coherence length (CCL) of 13.9 nm, and d-spacing of 19.6 Å), the (001) peak at 0.49 $Å^{-1}$ (with a CCL of 15.7 nm, and d-spacing of 12.8 Å), and the (010) peak at 1.60 $Å^{-1}$ (with a CCL of 10.5 nm, and d-spacing of 3.9 Å) evident in the data. Blending PQT with Bis-$PC_{61}BM$ leads to less ordered PQT packing, as evidenced by the sharp decrease in these signature peaks of PQT, but the development of a new structure is not evident. PQT:$PC_{61}BM$ blends showed quite different behavior. As seen in PQT-M1 thin films, a sharp reflection is seen at 0.197 $Å^{-1}$ (with a CCL of 19.6 nm, and d-spacing of 31.8 Å), indicating an increase in the lamellae spacing, suggesting the incorporation of $PC_{61}BM$ into the PQT forming bimolecular crystals, decreasing the interdigitation and forcing the PQT chains apart. It should be noted that two new peaks appeared at 0.66 $Å^{-1}$ (with a CCL of 17.9 nm, and d-spacing of 9.6 Å) and 1.75 $Å^{-1}$ (with a CCL of 9.4 nm, and d-spacing of 3.5 Å). The PQT π–π

stacking distance is ~3.9 Å and fullerene has a diameter of ~8.3 Å [25]. This suggests that 2-3 PQT layers could host one $PC_{61}BM$. The scattering peak at 0.66 $Å^{-1}$ is similar to the characteristic peak of pure $PC_{61}BM$ (Fig. S2), thus is assigned to $PC_{61}BM$ separation distance. And the 1.75 $Å^{-1}$ peak is assigned to a reorganized π–π stacking distance. Such a well-organized structure with better $PC_{61}BM$ ordering in the solid state would be expected to have good electron transport, but this is not the case. Fig. 1d and Fig. S3 showed the bilayer thin films (PQT was transfer printed onto $PC_{61}BM$ layers) at different thermal annealing temperatures for 15 min. Such a treatment should reveal structure details on the diffusion of $PC_{61}BM$ into PQT. PQT:$PC_{61}BM$ bilayers annealed at 85 ^oC showed a quite complicated structure, with a sharp primary reflection at 0.20 $Å^{-1}$ (with d-spacing of 31.4 Å), which we attribute to $PC_{61}BM$ diffusion induced bimolecular crystal formation, with even tighter packing than that seen in the BHJ thin film. Thermal annealing at 150 ^oC yielded a primary peak at 0.23 $Å^{-1}$ (with d-spacing of 27.3 Å), which is similar to solution preparation. These results indicate that PQT:$PC_{61}BM$ bimolecular crystals are a thermally-dynamic stable species. PQT:Bis-$PC_{61}BM$ bilayer experiments showed similar results as in solution prepared BHJ thin film. Thus Bis-$PC_{61}BM$ could only diffuse into PQT amorphous regions with thermal annealing.

In situ GIWAXS was used to measure the time evolution of the morphology of PQT:fullerene blends from the solution to the final film on drop-cast thin film, as shown in Fig. 2 and Fig. S4. The diffuse reflection at q~1.8 $Å^{-1}$ is attributed to the solvent and was used to assess the solvent evaporation from the film. As seen in the scattering profiles, a rapid decrease in the scattering occurs at frame 9 and vanishes by frame 13, indicating the conversion from a solution to a solid film. At frame 5, prior to the removal of all the solvent, the (100) reflection, characteristic of the bimolecular crystal is evident. As solvent evaporates (from frame 10 to 15), the distance corresponding to the (100) reflection decreases from 28 to 27 Å, indicating that the solvent has solubilized the side chains, increasing the interchain separation distance. Thus such state is even stable under solution condition, indicating a high entropy gain in its formation. The earlier state bimolecular crystal formation is slightly larger in interplane distance due to solvent molecule interruption. Liquid to solid-state transition leads to reorganization of bimolecular crystal organization, as seen from the interplane distance change from frame 10 to frame 15. A schematic presentation of such process was shown in Fig. 2d. PQT:Bis-$PC_{61}BM$ *in situ* experiment showed more complicated behavior. The liquid to solid-state transition was from frame 14 to 19. PQT in solution state can form little interdigitated (100) packing, as seen from a low inter-plane distance (~22 Å) at frame 5. This value then increased to ~27 Å at frame 10, indicating the formation of Bis-$PC_{61}BM$ incorporated bimolecular crystals. Such crystal is

not stable, which quickly decomposed towards PQT crystalline packing. PQT crystal and bimolecular crystal continued to form before the solidification, and then the low q region can be splitted into two peaks, as seen from hexagon and square symbols in data plots (Fig. 2c). When film get solidified (~frame 20), PQT:Bis-$PC_{61}BM$ bimolecular crystal quickly get decomposed, a strong PQT crystal formation process drive out the trace solvent and reorganize the side chain packing, which was stabilized at ~21 Å in the end. Such *in situ* experiments showed quite intriguing results regarding the bimolecular crystallization of different pairs. The PQT:$PC_{61}BM$ guest-host crystallization is stable, that can undergo thermal annealing and solvent etching; PQT:Bis-$PC_{61}BM$ can only form bimolecular crystals with the presence of solvent in loosely packed PQT state, which then decomposes quickly due to a more favorable PQT crystallization. Such a difference should be traced from their packing nature. In PQT:$PC_{61}BM$ blends, we noticed a strong bimolecular (100) packing, good PQT (010) packing, and good $PC_{61}BM$ (100) packing. Thus PQT:$PC_{61}BM$ bimolecular crystal is a simple fusion of PQT and $PC_{61}BM$ crystals, which form lamellae structure through favorable electronic interactions. PQT:Bis-$PC_{61}BM$ bimolecular crystal that is less favorable, which is due to the incompatibility of the PQT side chain and Bis-$PC_{61}BM$. The dual tail in Bis-$PC_{61}BM$ is less well defined in chemical structure, and thus hard to cocrystallize. Only under the presence of solvent molecules, the Bis-$PC_{61}BM$ can be trapped into the PQT lamellae. But during liquid to solid transition, there is no free energy gain between the two molecular layer reorganization, thus leading to the PQT side chain interdigitation and pushing Bis-$PC_{61}BM$ out, further decomposing the bimolecular crystal. Such process was shown in Fig. 2e in detail.

We then investigate the phase separation of the two pairs of BHJ thin films, which is an important factor that affects the device performance. Fig. 3 shows the transmission electron microscopy (TEM), resonant soft x-ray scattering (RSoXS), and grazing incident small angle x-ray scattering (GISAXS) data, which were used to investigate the bulk morphology and phase separation scale of blends. As shown in Fig. 3a, the PQT-M1 and PQT-M2 showed a homogeneous morphology with small sized phase separation. While the PQT-M3 blends showed a large length scale of phase separation around 100 nm. The PQT-M4 blends showed larger domains, which composed of Bis-$PC_{61}BM$ aggregations. RSoXS experiment was conducted (Fig. 3b and Fig. S5) to provide the phase separation statistics using 284.2 eV photon energy. PQT-M1 blends showed a scattering hump at 0.015 $Å^{-1}$, giving a distance of 42 nm. PQT-M2 blends showed less pronounced phase separation with a quite broad size distribution. PQT:Bis-$PC_{61}BM$ blends showed quite strong Bragg scattering peaks, 0.006 $Å^{-1}$ for PQT-M3 (distance of 105 nm) and 0.005 $Å^{-1}$ for PQT-M4 (distance of 125 nm). Fig. 3c showed the

GISAXS profiles of PQT:fullerene blends that covers larger q range. Quit similar results were obtained from GISAXS profiles [26]. The GISAXS profile of PQT-M1 shows a broad diffuse peak at ~0.015 $Å^{-1}$, giving a phase separation of ~42 nm. While for the PQT-M2, there is no scattering peak in the GISAXS profiles due to the indistinguishable phase. For PQT-M3 and PQT-M4, both the phase separation and phase contrast are obvious, which results in the GISAXS profiles with obvious scattering peaks at around ~0.0075 $Å^{-1}$ and ~0.006 $Å^{-1}$, corresponding d-spacing of 81 and 105 nm, respectively. The length scale of phase separation is slightly smaller than that shown in TEM images and RSOXS data due to the inaccuracy of reading scattering peak position resulted from the incomplete shape of peaks.

In augment to study the phase separation of blends, RSoXS can be used to characterize the scattering anisotropy caused by the locally ordered structure, thus determining the interfacial molecular orientation [27-29]. We take the PQT-M4 system as an example due to its clear phase separation. As can be seen from Fig. 4a, the change in photon energy and electric field direction of polarized x-rays leads to drastically different scattering anisotropy, which can be assessed by the factor $\sigma = (I_{90} - I_{180})/(I_{90} + I_{180})$ that shown in Fig. S6 [30-32]. Under the s polarization x-ray, the scattering intensity in the vertical direction was greatly enhanced at 285.0 eV (σ=0.17), which is ascribed to the polymer 1s-π^* transition. On photon energy at 287.3 eV that of polymer 1s-σ^* transition, polarization factor changed to -0.29. This result assumes an edge-on orientation of PQT polymer on the Bis-$PC_{61}BM$ surface. While for the x-ray energy far below or above the absorption edge of polymer (285 eV), the scattering images became less anisotropic. By turning the x-rays from s-polarization to p-polarization, the scattering anisotropy changed correspondingly. Fig. 4b presents the schematic of scattering anisotropy under different polarized x-rays (s-polarization, and p-polarization). It can be seen that varying the electric directions of polarized x-rays accordingly change the scattering intensity in different directions.

To investigate the relationship between molecular packing and the device performance, the solution-processed BHJ organic solar cells were fabricated with the PQT as the electron donor and $PC_{61}BM$ or Bis-$PC_{61}BM$ as the electron acceptor using a conventional device structure of indium-tin oxide (ITO)/poly (3,4-ethylenedioxythiophene):poly(styrenesulfonate) (PEDOT:PSS)/BHJ blends/Al (Fig. 5a). Fig. 5b show the photocurrent-voltage (*J-V*) curves of devices with PQT:fullerene as active layers, and the detailed device parameters (J_{SC}, V_{OC}, FF, and PCE) is presented in Table S1. The data show a strong dependence of the device performance on the PQT:fullerene weight ratios and electron acceptors. PQT-M1 blends based device showed an inferior device performance with a low V_{OC} of 0.46 eV. Such value is well

below that from polythiophene based donor polymers. While large amount of PQT would participate in bimolecular crystals, leaving amorphous PQT mixed with $PC_{61}BM$ to form a low-density acceptor domain. Such a BHJ structure though can form a reasonable phase separation, is electronically not ideal to generate carriers. Bimolecular crystal with high presence of $PC_{61}BM$ loading could lead to serious quenching issues, and electron transport in mixing region would also be poor. These reasons contribute to a low FF and small J_{SC}. For PQT-M2 blends, the best device showed a PCE of 0.96%, which is four times that of PQT-M1 blends based device. A V_{oc} of 0.74 V was recorded, which is well above polythiophne:$PC_{61}BM$ blends. The power output voltage increase indicates a fundamental change in electronic structure that constitutes the BHJ functioning domains. High $PC_{61}BM$ loading makes the electron transporting quite efficient, and it is expected that the bimolecular crystal in this condition could form as the electron donor, which the hybrid new LUMO becomes deepened, leading to a V_{OC} increase. PQT-M4 blends showed a V_{OC} of 0.66 V and a J_{SC} of 2.28 mA/cm^2, which is in normal parameter space. Adding more Bis-$PC_{61}BM$ leads to the decrease of V_{OC} and J_{SC}, which is in reverse to PQT:$PC_{61}BM$ blends. While in this blends PQT and Bis-$PC_{61}BM$ could form well-structured phase separation, the decrease in V_{OC} is expected by the electronic structure change of amorphous PQT:Bis-$PC_{61}BM$ mixing domains.

In order to investigate the effects of molecular packing on the electron transport properties [33], perovskite solar cells with different PQT:$PC_{61}BM$ weight ratios as an electron transporting layer (ETL) were fabricated. The device structure of perovskite solar cells is shown in Fig. 5a. The PTAA was deposited on ITO glass substrate as hole transporting layer. $MAPbI_3$ was spin-coated using antisolvent engineering techniques [34, 35]. Then PQT:$PC_{61}BM$ ETL was spin coated on the perovskite film. Fig. 5c shows the *J-V* curves of perovskite solar cells with varied weight ratios of PQT:$PC_{61}BM$ as electron transporting layer, and the corresponding device parameters are given in Table S2. Detailed distribution of performance parameters (PCE, J_{SC}, V_{OC}, and FF) are shown in Fig. S7. It is clear that the amount of PQT significantly affects the device performance. PQT:$PC_{61}BM$ 1:1 blends showed a quite poor device performance, with quit low V_{OC} and J_{SC}. Such results is much poorer comparing to cases that using P3HT:$PC_{71}BM$ blends as the electron transporting layers [36]. Thus bimolecular crystal is not a good electron transporting media. We then start to increase $PC_{61}BM$ loading. 1:2 blends showed a significant improvement, showing quit improved J_{SC}, V_{OC} and FF. It thus indicates in this condition $PC_{61}BM$ could start to form a good transporting pathway. With the weight ratio decreasing to 1:8, a higher efficiency was achieved, with a champion efficiency of 16.68% (Fig. 5d), which is comparable to pure PCBM transporting layers. However, under such condition quite high

hysteresis was recorded, indicating that bimolecular crystal can be of issue in blocking and switching transport in perovskite solar cells.

Conclusions

In summary, the current work demonstrate the instability, kinetics of PQT:$PC_{61}BM$/Bis-$PC_{61}BM$ bimolecular crystals and their function in BHJ solar cells and electron transporting layers. It is shown PQT:$PC_{61}BM$ bimolecular crystal is thermal-dynamic drive, while PQT:Bis-$PC_{61}BM$ bimolecular crystal is intrinsically unstable that could only exist when solvent in presence. Both the molecular packing and the length scale of phase separation in polymer:fullerene BHJ film have a significant effect on the device performance. In the case of PQT:$PC_{61}BM$, a stable and ordered bimolecular crystal assumes large amount of $PC_{61}BM$, thus a high $PC_{61}BM$ loading is necessary to achieve good electron transport and making bimolecular domain functioning as a whole electron donor, thus carriers generated from bimolecular crystal domain can be extracted. For the PQT:Bis-$PC_{61}BM$ blends, it is easy to form a bicontinuous BHJ morphology, yet it should be noted that PQT crystalline order is poor. There is strong interfacial orientation existed between PQT rich domain and Bis-$PC_{61}BM$ rich domain, the interface get smoothed when more Bis-$PC_{61}BM$ is presented, which yet leads to decrease in device performance but better FF. Good electron transporting ability is obtained when PQT:$PC_{61}BM$ blending ratio reaches 1:8, which can then be used in perovskite solar cells as electron transporting layers. Our work can provide the guidance for how to design the effective active layer materials and electron transporting layer by controlling the polymer:fullerene ratios.

Experimental Section

Materials

Poly(3,4-ethylenedioxythiophene):poly(styrenesulfonate) (PEDOT:PSS, PVP AI4083) was purchased from Heraeus Clevios. Poly(3, 3’-didodecylquaterthiophene) (PQT) was

purchased from American Dye Source, Inc. Both phenyl-C61-butyric acid methyl ester ($PC_{61}BM$) and its derivatives (Bis-$PC_{61}BM$) were ordered from Solarmer, with the purity of 99.5%. The poly(bis(4-phenyl)(2,4,6-trimethylphenyl)amine) (PTAA) were purchased from Xi'an Polymer Light Technology Corp. Lead iodide (PbI_2, 98%) was purchased from TCI, and methylammoniumthe iodide (MAI, 99.998%) was bought from Deysol. All the solvents were purchased from Acros, and used as received.

Solar cell fabrication

The BHJ solar cells were fabricated with a device structure of ITO/PEDOT:PSS/PQT:fullerene/Al. ITO glasses with a sheet resistance ≤10 Ω cm^{-2} was consecutively ultra-sonicated in detergent, deionized water, acetone and isopropanol for 15 min, respectively, and then dried at 70 ^oC for overnight. After UV-Ozone treatment for 15 min, the PEDOT:PSS was spin-coated onto the ITO glass at 3800 rpm for 30 s, and annealed at 150 ^oC for 15 min. Then the substrate was transferred into glovebox for further device fabrication. The precursor solutions of PQT:fullerene ($PC_{61}BM$ and Bis-$PC_{61}BM$) with different weight ratios were spin-coated at 2000 rpm for 40 s onto the PEDOT:PSS layer. After deposition of the active layer, the sample was transferred into a vacuum chamber for further deposition of 100 nm Al to finish the device fabrication process. To evaluate the electron transfer characteristic of bimolecular crystals, we fabricated perovskite solar cells with a device structure of ITO/PTAA/$MAPbI_3$/PQT:$PC_{61}BM$/Al. Firstly, the PTAA with a concentration of 2 mg/ml was spin coated on the UV-Ozone treated ITO glass at 5000 rpm for 30 s, then thermal annealed at 150 ^oC for 10 min. To improve the wetting property of the perovskite precursor solution, the PTAA film was pre-wetted by spinning 70 μl DMF at 4000 rpm for 10 s. Subsequently, the perovskite precursor solution (MAI:PbI_2=1:1.08 was dissolved into the mixed DMF:DMSO solution, with volume ratio of 9:1) was spun coated at 4000 rpm for 30s, and then the anti-solvent chlorobenzene was drop onto the films at 22 s before the end the spin-coating step, followed by a thermal annealing treatment at 100 ^oC for 10 min. After the film cooled to room temperature, the PQT:$PC_{61}BM$ with different weight ratios (15 mg/ml, 0:1, 1:1, 1:2, 1:4, 1:6, 1:8) was spin coated on the perovskite film at 2000 rpm for 30 s as electron transporting layer. Finally, the 100 nm Al electrode was evaporated in a vacuum chamber.

Film characterization

The UV-vis absorption spectra were measured by a Lambda 750 instrument in Perkin Elmer model. Grazing incidence wide and small angle x-ray scattering (GIWAXS, GISAXS) measurements were conducted at beamline 7.3.3, Advanced Light Source (ALS), Lawrence Berkeley National Lab (LBNL). The wavelength of x-ray was 1.24 Å and the incident angle of

x-ray was fixed to 0.16° with respect to the substrate. Resonant soft x-ray scattering (RSoXS) was performed at beamline 11.0.1.2, Lawrence Berkeley National Lab. Thin films was flowed and transferred onto Si_3N_4 substrate, and experiment was done in transmission mode. Bright-field transmission electron microscopy (TEM) experiments were conducted with a JEOL 2000 FX TEM operating at an accelerating voltage of 200 kV.

In situ GIWAXS characterization

Before experiment, the mini slot die instrument was installed in a helium box. Then a surveillance camera was used to monitor the solvent flow from the slot die head. Before the coating started, the substrate is pre-aligned and a 0.16° incident angle is used in GIWAXS experiment. As soon as the solution went out, the coating process started immediately. At the same time, the structural information was recorded with typical exposure time of 30 s for each frame in a burst mode.

Device characterization

The photovoltaic device performance was analyzed by the Keithley 2400 Instrument under a 150 W solar simulator (XES-40S2-CE, SAN-EI Electric Co. Ltd.) equipped with AM 1.5G filter. The light intensity was calibrated to 100 mW cm^{-2} with a standard monocrystalline silicon reference cell (AK-2000, KONICA MINOLTA, INC, Japan).

References

1 K. Li, Y. Wu, Y. Tang, M. A. Pan, W. Ma, H. Fu, C. Zhan, J. Yao, Adv. Energy Mater. 2019, 9, 1901728.

2 B. Fan, D. Zhang, M. Li, W. Zhong, Z. Zeng, L. Ying, F. Huang, Y. Cao, Sci. China Chem. 2019, 62, 746.

3 Q. An, X. Ma, J. Gao, F. Zhang, Sci. Bull. 2019, 64, 504.

4 Y. Cui, H. Yao, J. Zhang, T. Zhang, Y. Wang, L. Hong, K. Xian, B. Xu, S. Zhang, J. Peng, Z. Wei, F. Gao, J. Hou, *Nat. Commun*. **2019**, *10*, 2515.

5 J. Yuan, Y. Zhang, L. Zhou, G. Zhang, H.-L. Yip, T.-K. Lau, X. Lu, C. Zhu, H. Peng, P. A. Johnson, M. Leclerc, Y. Cao, J. Ulanski, Y. Li, Y. Zou, *Joule* **2019**, *3*, 1140.

6 L. Zhu, W. Zhong, C. Qiu, B. Lyu, Z. Zhou, M. Zhang, J. Song, J. Xu, J. Wang, J. Ali, W. Feng, Z. Shi, X. Gu, L. Ying, Y. Zhang, F. Liu, *Adv. Mater*. **2019**, *31*, e1902899.

7 Z. Zhou, S. Xu, J. Song, Y. Jin, Q. Yue, Y. Qian, F. Liu, F. Zhang, X. Zhu, *Nat. Energy* **2018**, *3,* 952.

8 Z. Xiao, X. Jia, L. Ding, *Sci. Bull.* **2017**, *62*, 1562.

9 A. C. Mayer, M. F. Toney, S. R. Scully, J. Rivnay, C. J. Brabec, M. Scharber, M. Koppe, M. Heeney, I. McCulloch, M. D. McGehee, *Adv. Func. Mater.* **2009**, *19*, 1173.

10 J. Song, M. Zhang, M. Yuan, Y. Qian, Y. Sun, F. Liu, *Small Methods* **2018**, *2*, 1700229.

11 Y.-W. Su, S. -C. Lan, K. -H. Wei, *Mater. Today* **2012**, *15*, 554.

12 N. C. Miller, E. Cho, M. J. Junk, R. Gysel, C. Risko, D. Kim, S. Sweetnam, C. E. Miller, L. J. Richter, R. J. Kline, M. Heeney, I. McCulloch, A. Amassian, D. Acevedo-Feliz, C. Knox, M. R. Hansen, D. Dudenko, B. F. Chmelka, M. F. Toney, J. L. Bredas, M. D. McGehee, *Adv. Mater*. **2012**, *24*, 6071.

13 A. P. Yuen, J. S. Preston, A. -M. Hor, R. Klenkler, E. Q. B. Macabebe, E. Ernest van Dyk, R. O. Loutfy, *J. Appl. Phys.* **2009**, *105*, 016105.

14 M. Koppe, M. Scharber, C. Brabec, W. Duffy, M. Heeney, I. McCulloch, *Adv. Func. Mater*. **2007**, *17*, 1371.

15 J. E. Parmer, A. C. Mayer, B. E. Hardin, S. R. Scully, M. D. McGehee, M. Heeney, I. McCulloch, *Appl. Phys. Lett.* **2008**, *92*, 113309.

16 Thompson, B. C.; Kim, B. J.; Kavulak, D. F.; Sivula, K.; Mauldin, C.; Frechet, J. M. J. Influence of Alkyl Substitution Pattern in Thiophene Copolymers on Composite Fullerene Solar Cell Performance. Macromolecules 2007, 40, 7425.

17 N. C. Miller, R. Gysel, C. E. Miller, E. Verploegen, Z. Beiley, M. Heeney, I. McCulloch, Z. Bao, M. F. Toney, M. D. McGehee, *J. Polym. Sci. Part B: Polym. Phys.* **2011**, *49*, 499.

18 D. Chirvase, J. Parisi, J. C. Hummelen, V. Dyakonov, *Nanotechnology* **2004**, *15*, 1317.

19 T. Erb, U. Zhokhavets, G. Gobsch, S. Raleva, B. Stühn, P. Schilinsky, C. Waldauf, C. J. Brabec, *Adv. Func. Mater.* **2005**, *15*, 1193.

20 A. P. Yuen, A.-M. Hor, S. M. Jovanovic, J. S. Preston, R. A. Klenkler, N. M. Bamsey, R. O. Loutfy, *Sol. Energy Mater. Sol. Cells* **2010**, *94*, 2455.

21 G. Wantz, F. Lefevre, M. T. Dang, D. Laliberté, P. L. Brunner, O. J. Dautel, *Sol. Energy Mater. Sol. Cells* **2008**, *92*, 558.

22 R. J. Kline, D. M. DeLongchamp, D. A. Fischer, E. K. Lin, L. J. Richter, M. L. Chabinyc, M. F. Toney, M. Heeney, I. McCulloch, *Macromolecules* **2007**, *40*, 7960.

23 S. Cook, H. Ohkita, Y. Kim, J. J. Benson-Smith, D. D. C. Bradley, J. R. Durrant, *Chem. Phys. Lett.* **2007**, *445*, 276.

24 C. Gong, Q. L. Song, H. B. Yang, J. Li, C. M. Li, *Sol. Energy Mater. Sol. Cells* **2009**, *93*, 1928.

25 M. Williams, N. R. Tummala, S. G. Aziz, C. Risko, J. -L. Bredas, *J. Phys. Chem. Lett.* **2014**, *5*, 3427.

26 M. -S. Su, C. -Y. Kuo, M. -C. Yuan, U. -S. Jeng, C. -J. Su, K. -H. Wei, *Adv. Mater.* **2011**, *23*, 3315.

27 N. C. Miller, S. Sweetnam, E. T. Hoke, R. Gysel, C. E. Miller, J. A. Bartelt, X. Xie, M. F. Toney, M. D. McGehee, *Nano Lett*. **2012**, *12*, 1566.

28 F. Liu, M. A. Brady, C. Wang, *Eur. Poly. J.* **2016**, *81*, 555.

29 F. Liu, Y. Gu, C. Wang, W. Zhao, D. Chen, A. L. Briseno, T. P. Russell, *Adv. Mater.* **2012**, *24*, 3947.

30 B. A. Collins, J. E. Cochran, H. Yan, E. Gann, C. Hub, R. Fink, C. Wang, T. Schuettfort, C. R. McNeill, M. L. Chabinyc, H. Ade, *Nat. Mater.* **2012**, *11*, 536.

31 F. Liu, C. Wang, J. K. Baral, L. Zhang, J. J. Watkins, A. L. Briseno, T. P. Russell, *J. Am. Chem. Soc.* **2013**, *135*, 19248.

32 C. Zhu, C. Wang, A. Young, F. Liu, I. Gunkel, D. Chen, D. Walba, J. Maclennan, N. Clark, A. Hexemer, *Nano Lett.* **2015**, *15*, 3420.

33 H. -K. Lin, Y. -W. Su, H. -C. Chen, Y. -J. Huang, K. -H. Wei, *ACS Appl. Mater. Interfaces* **2016**, *8*, 24603.

34 M. Xiao, F. Huang, W. Huang, Y. Dkhissi, Y. Zhu, J. Etheridge, A. Gray-Weale, U. Bach, Y. B. Cheng, L. Spiccia, *Angew. Chem.* **2014**, *53*, 9898.

35 K. Chen, Q. Hu, T. Liu, L. Zhao, D. Luo, J. Wu, Y. Zhang, W. Zhang, F. Liu, T. P. Russell, R. Zhu, Q. Gong, *Adv. Mater*. **2016**, *28*, 10718.

36 Z. Xu, L.-M. Chen, G. Yang, C.-H. Huang, J. Hou, Y. Wu, G. Li, C.-S. Hsu, Y. Yang, *Adv. Func. Mater*. **2009**, *19*, 1227.

Conflicts of interest

There are no conflicts of interest to declare.

Acknowledgements

This work was financially supported by the Young 1000 Talent Program of China, the National Natural Science Foundation of China (NSFC) (Nos. 51973110, 21734009, 21905102 and 61805138). Portions of this research were carried out at beamline 7.3.3 and 11.0.1.2 at the Advanced Light Source, Molecular Foundry, and National Center for Electron Microscopy, Lawrence Berkeley National Laboratory, which was supported by the DOE, Office of Science, and Office of Basic Energy Sciences. Q. H. and T. P. R. were supported by the US Office of Naval Research under contract N00014-17-1-2241.

Figures and captions

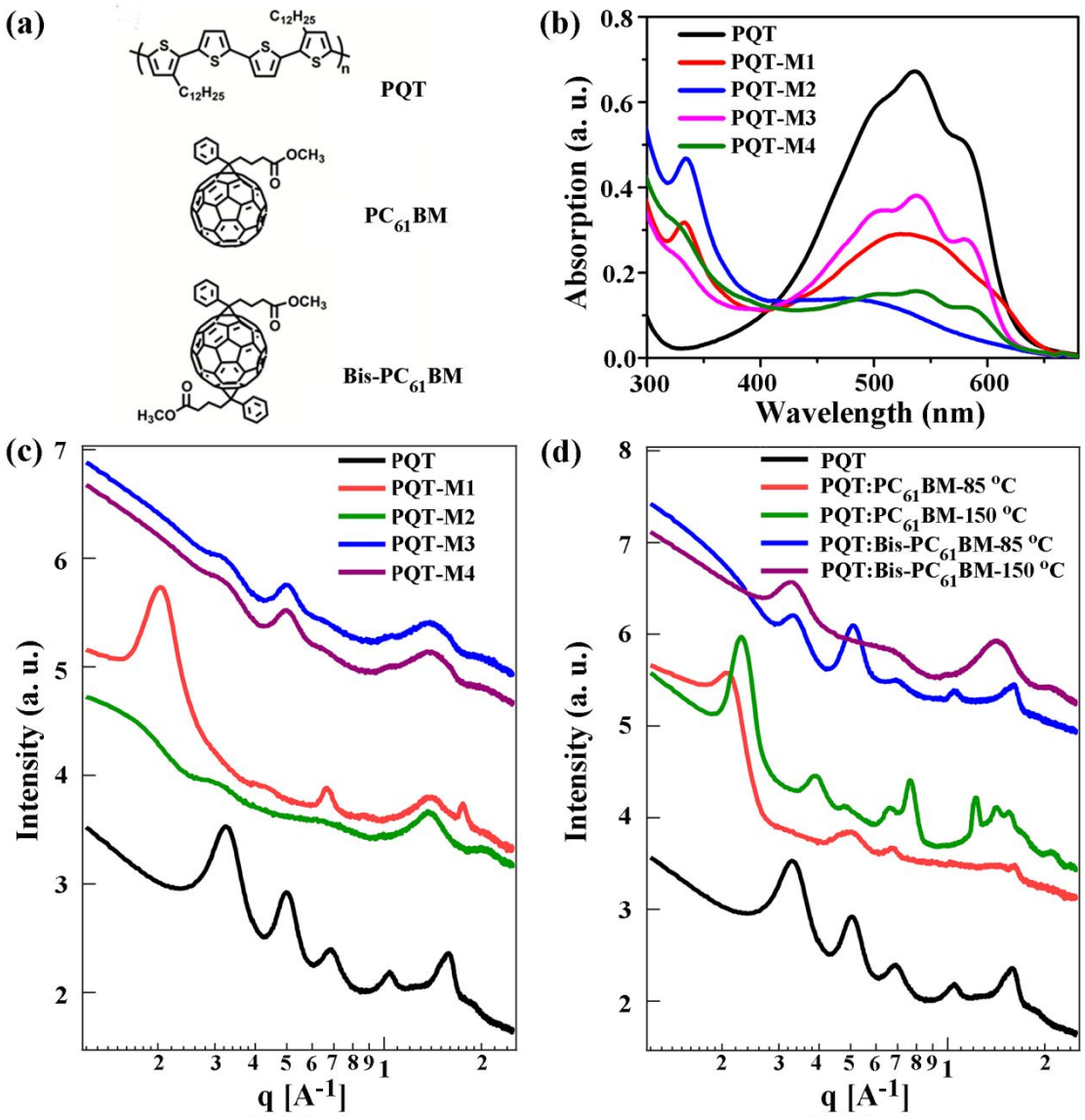

Fig. 1 (a) Chemical structure of poly(3, 3’’’-didodecylquaterthiophene) (PQT), [6, 6] phenyl C61 butyric acid methyl ester ($PC_{61}BM$), and $PC_{61}BM$ bisadduct (Bis-$PC_{61}BM$). (b) UV-vis absorption spectra of pristine PQT, PQT-M1, PQT-M2, PQT-M3, and PQT-M4. (c) Grazing incident wide angle x-ray scattering (GISAXS) profiles of pristine PQT, PQT-M1, PQT-M2, PQT-M3, and PQT-M4. (d) GIWAXS profiles of bilayer thin films treated at different thermal annealing temperatures to investigate the diffusion of fullerene ($PC_{61}BM$, and Bis-$PC_{61}BM$) into PQT.

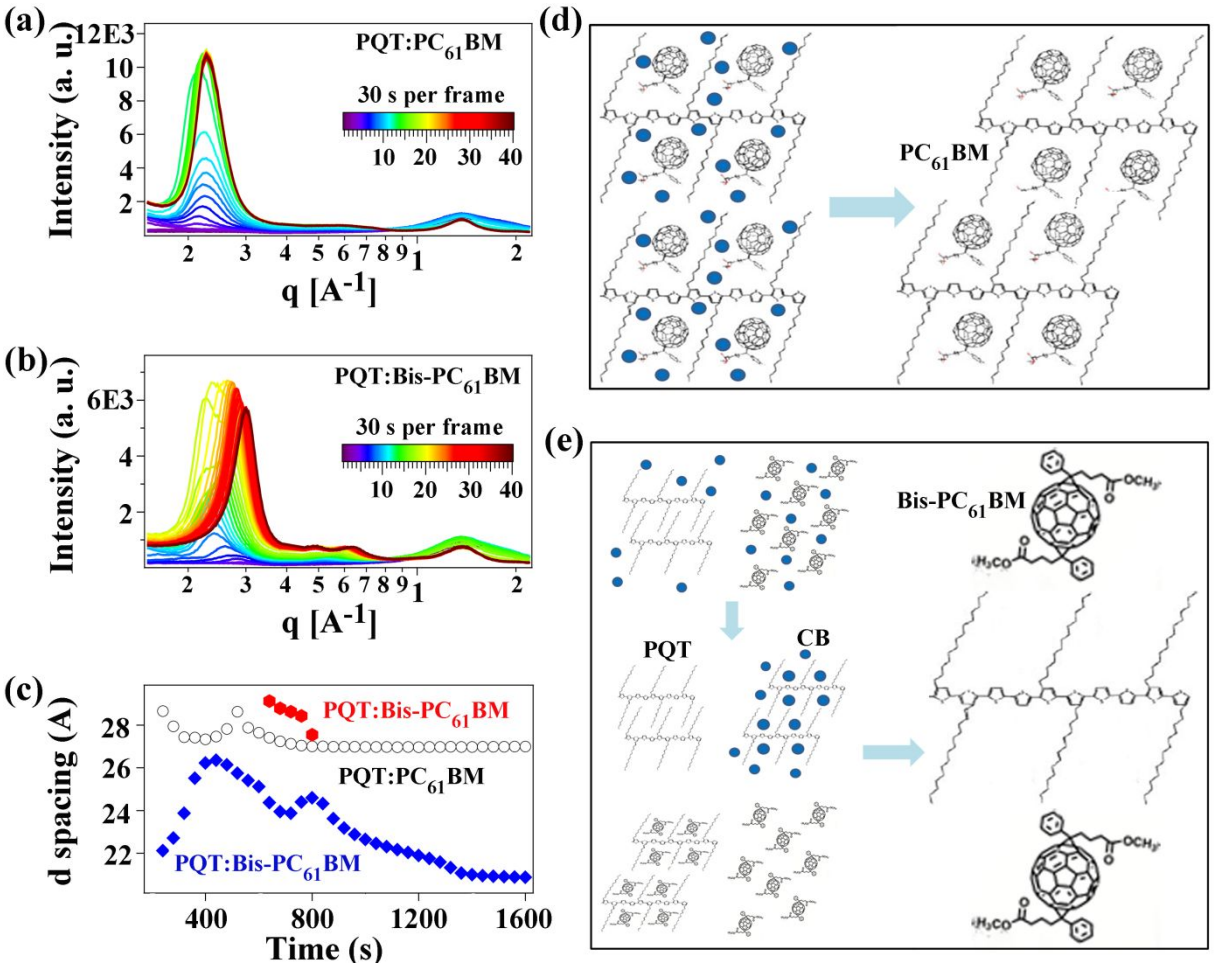

Fig. 2 *In situ* 1D GIWAXS profiles of PQT:PC_{61}BM (a) and PQT:Bis-PC_{61}BM (b) drying along with time (40 frames, 30 s per frame). (c) The corresponding evolution of lamellae stacking distance along with time. Schematic models showing the formation kinetics of PQT:PC_{61}BM (d) and PQT:Bis-PC_{61}BM (e).

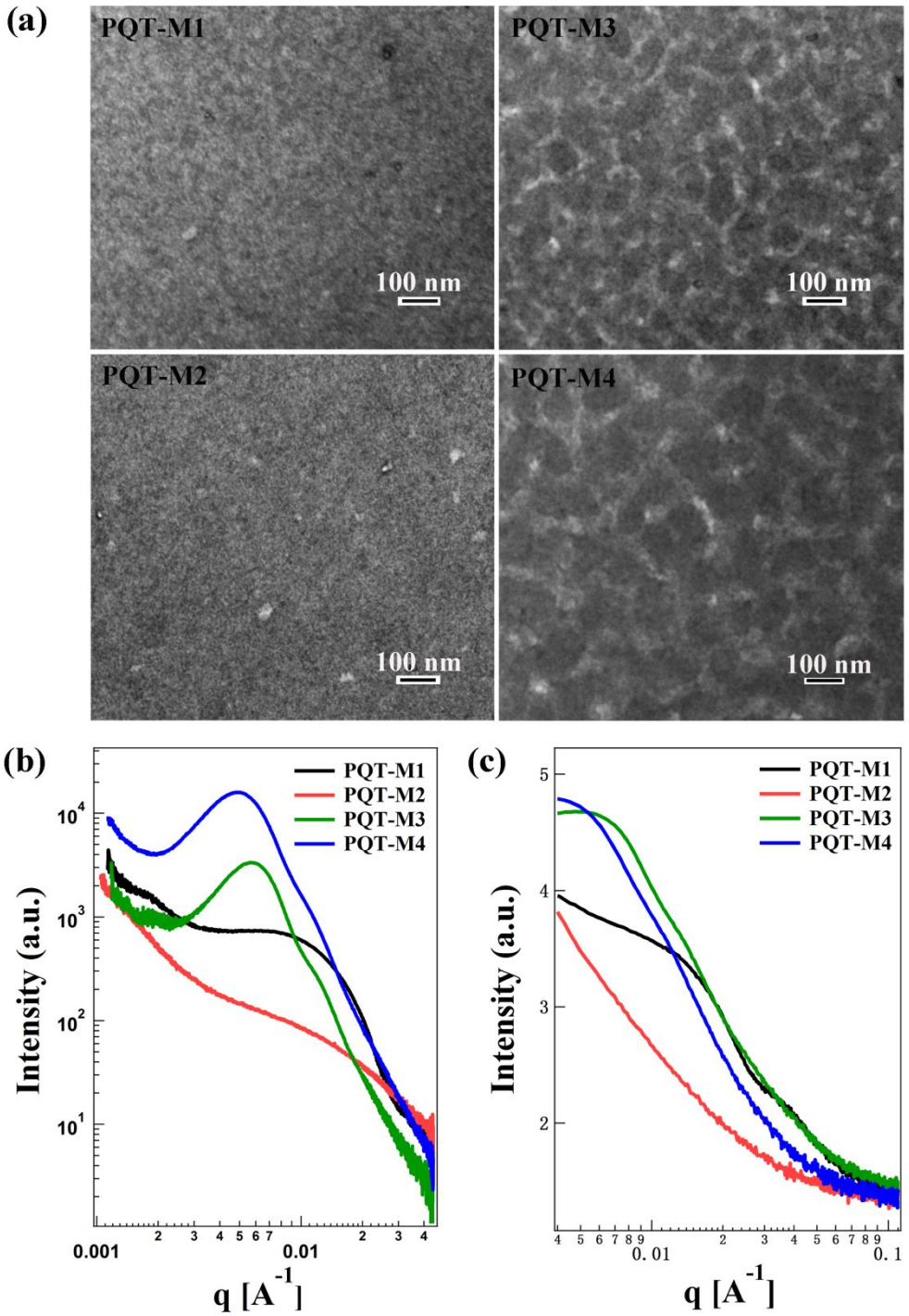

Fig. 3 (a) Transmission electron microscopy (TEM) images, (b) resonant soft X-ray scattering (RSoXS), and (c) grazing incident small angle x-ray scattering (GISAXS) of PQT-M1, PQT-M2, PQT-M3, and PQT-M4.

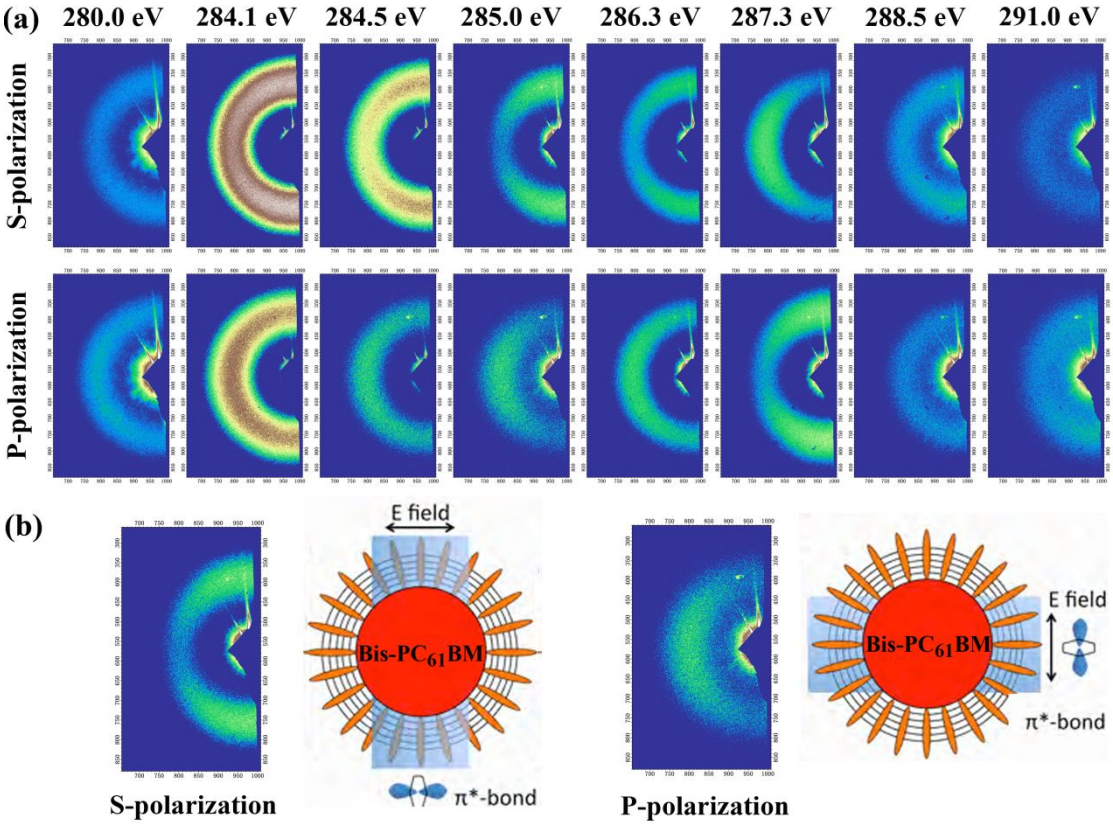

Fig. 4 (a) Energy and polarization dependent transmission RSoXS images of PQT-M4 blends across the carbon 1s edge, showing the scattering anisotropy near the π* and σ* transitions, as well as the local molecular orientation. (b) Polarization dependent scattering patterns of PQT-M4 films.

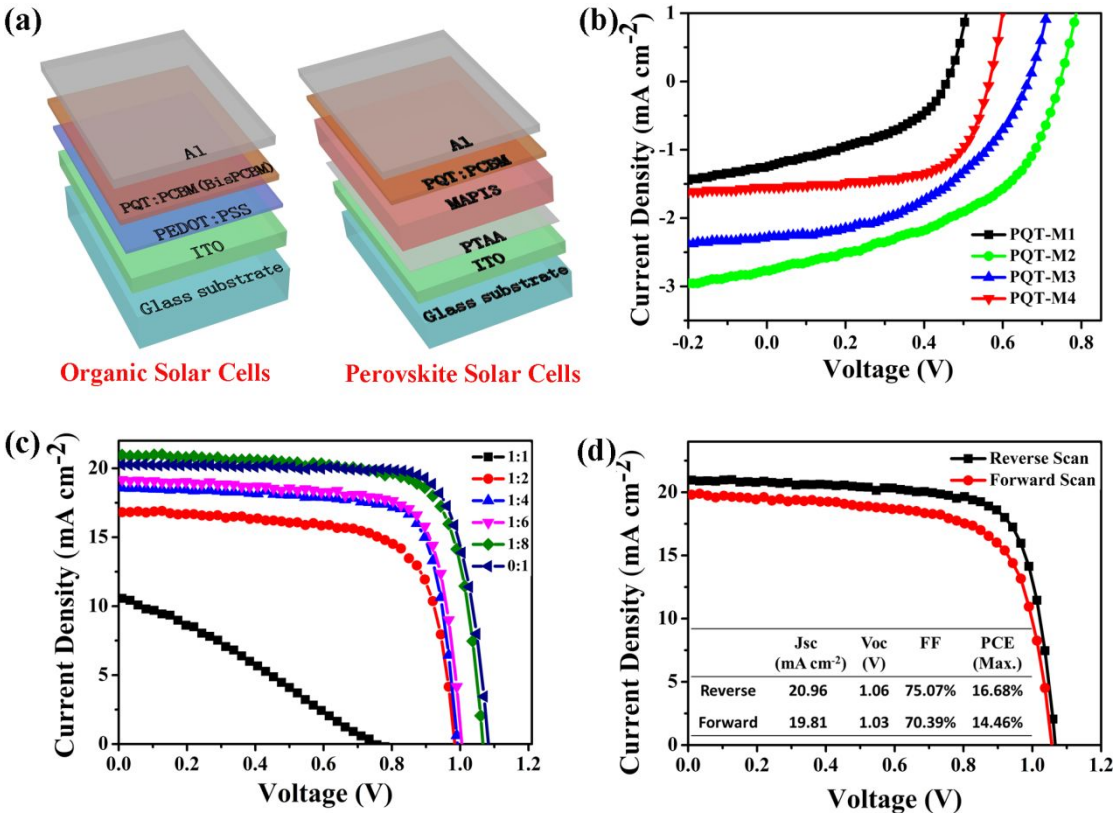

Fig. 5 (a) A schematic representation of the device configuration of bulk-heterojunction (BHJ) organic solar cells and perovskite solar cells. (b) Photocurrent-voltage (*J-V*) curves of the BHJ solar cells based on different active layers (PQT-M1, PQT-M2, PQT-M3, and PQT-M4). (c) *J-V* curves of perovskite solar cells with different PQT:$PC_{61}BM$ weight ratios as electron transporting layers. (d) *J-V* curves of a champion perovskite device measured in both forward and reverse directions. The inset table shows the detailed device parameters.

TOC

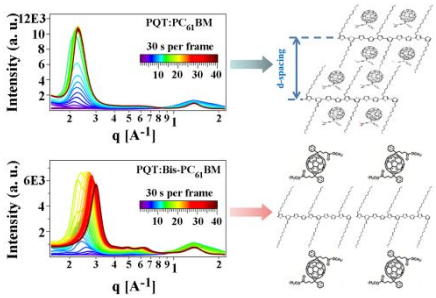

The *in situ* crystallization study reveals that size compatibility plays a key role in governing the formation of bimolecular crystals.